Tight Coupling of Laser Scanner and Inertial Measurements for a Fully Autonomous Relative Navigation Solution

Andrey Soloviev, Dustin Bates and Frank van Graas
Avionics Engineering Center
231 Stocker Center
Athens, Ohio 45701
USA

soloviev@ohio.edu

ABSTRACT

The paper describes a fully autonomous relative navigation solution for urban environments (indoor and outdoor). The navigation solution is derived by combining measurements from a two-dimensional (2D) laser scanner with measurements from inertial sensors. Navigation relies on the availability of structures (lines and surfaces) within the scan range (80 m, typically). Features (e.g. lines and corners) are first extracted from 2D laser scans and then used for position and heading determination. Inertial navigation states (position, velocity and attitude) are applied to predict feature displacements between laser scans, computationally adjust a 2D scan plane for tilting of the scanner platform, and to coast through scans where features extracted from scan images do not provide sufficient information for navigation. Parameters of features extracted from scan images are applied to periodically re-calibrate inertial states in order to reduce the error drift of inertial navigation parameters. The calibration herein uses a Kalman filter that performs a range-domain fusion of laser scanner and inertial data.

Indoor and outdoor live data test results are used to demonstrate performance characteristics of the laser/inertial integrated navigation. Positioning at the cm-level is demonstrated for indoor scenarios where well-defined features and good feature geometry are available. Test data from challenging urban environments show position errors at the meter-level after approx. 200 m of travel (between 0.6% and 0.8% of distance travelled).

1.0 INTRODUCTION

Outdoor localization services based on Global Navigation Satellite Systems (GNSSs) have tremendously matured over the past decade and are widely available in a variety of applications. Current GNSS user performance, however, is degraded by environmental boundaries. GNSS performance is generally sufficient for most localization applications in rural and suburban environments. In contrast, urban indoor and outdoor application areas still pose a very challenging environment for most GNSS receivers. When not integrated with other sensors, their performance is degraded. This paper thus addresses an application area that can be generally described as GNSS denied navigation for indoor and outdoor urban applications where man made obstacles attenuate GNSS signals to the level where they cannot be used for navigation. While man made obstacles represent a significant challenge for a GNSS-based localization, they can be efficiently used as localization reference points if their navigation-related features are detected and feature parameters are estimated.

Soloviev, A.; Bates, D.; van Graas, F. (2007) Tight Coupling of Laser Scanner and Inertial Measurements for a Fully Autonomous Relative Navigation Solution. In *Military Capabilities Enabled by Advances in Navigation Sensors* (pp. 4-1 – 4-30). Meeting Proceedings RTO-MP-SET-104, Paper 4. Neuilly-sur-Seine, France: RTO. Available from: http://www.rto.nato.int.

A laser scanner is employed to detect features that are associated with man-made obstacles. The scanner measures distances to reflecting surrounding objects in a certain angular range. Scanner operations are based on a time-of-flight measurement principle. The laser scanner sends out a pulse which returns to the scanner if reflected by an object in the scanner measurement range. The time-of-flight recorded is applied to estimate the distance to a reflecting object. The use of a rotating mirror allows for capturing object reflections in a certain angular range. Figure 1 illustrates operations of a two-dimensional (2D) laser scanner.

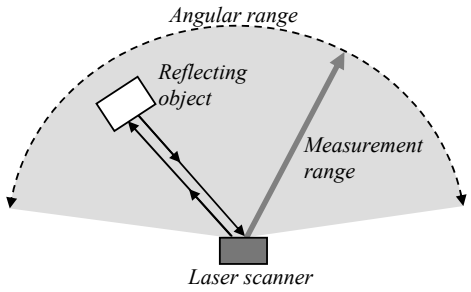

Figure 1: 2D Laser Scanner Measurements

Figure 2 illustrates principles of laser scanner-based navigation. Accordingly, a laser scanner is used to obtain images of surroundings (scan images). Features that are created by reflecting objects are then extracted from scan images. Changes in feature parameters are applied for navigation.

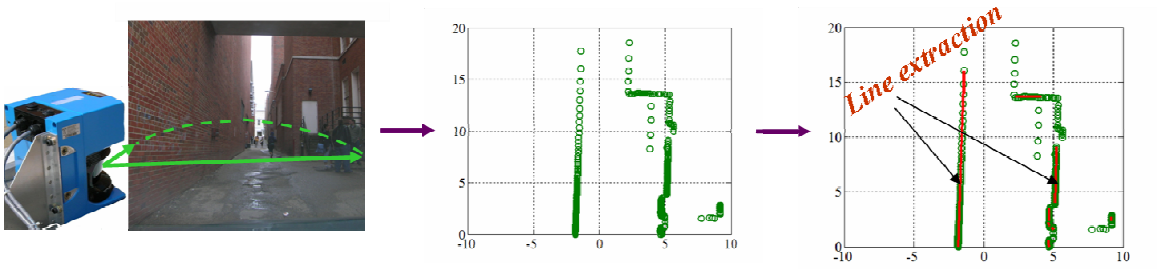

Figure 2: Laser Scanner-Based Navigation

A particular implementation scenario considered in this paper is a fully autonomous 2D relative positioning that is based on measurements of 2D laser scanner and Inertial Navigation System (INS) measurements. The navigation solution herein is computed in a local coordinate frame that is defined by the scanner position and orientation at the initial scan as illustrated in Figure 3.

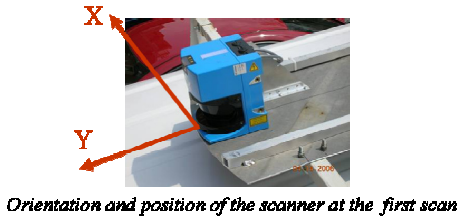

Figure 3: Relative Navigation Frame

A relative navigation solution is thus provided. Estimating local frame position and orientation in one of commonly used navigation frames (e.g. East-North-Up and Earth-Centered-Earth-Fixed frames) allows for the transformation of the relative navigation solution into an absolute navigation solution. Navigation herein is performed in completely unknown environments. No map information is assumed to be available *a priori*.

INS outputs are used to predict feature displacements between scans in order to improve feature matching, to compensate for tilt of the laser scanner platform, and to coast through cases where not enough features are extracted to compute the laser-based navigation solution.

In order to reduce drift in inertial navigation outputs, the INS is calibrated using parameters of features extracted from scan images. The calibration is performed in the measurement domain (i.e. using feature parameters) rather than using laser-based derived position and orientation. This integration approach is generally referred to as tight coupling.

The remainder of the paper is organized as follows. Previous efforts in the area of the laser scanner-based navigation are first summarized. Next, a 2D navigation mechanization that is based on 2D scan images is discussed. An INS-based compensation of laser scanner tilt angles that eliminates constraints on the scanner angular motion is then described. Next, a tight laser scanner/INS coupling scheme is provided. Results of live data tests for indoor and urban outdoor scenarios are used to demonstrate performance characteristics of the integrated laser/inertial navigation. Finally, the conclusion section summarizes the main results achieved.

2.0 PREVIOUS WORK

The majority of previous research related to this area has been for robotic localization with most approaches attempting to improve solutions to the so-called Simultaneous Localization and Mapping (SLAM) problem. SLAM using 2D laser scans has been performed using a number of different methods such as using extracted corners formed by the intersection of two walls [1], extracted lines [2], [3], [4], and in conjunction to retro-reflective beacons in known or unknown locations [5]. Although some work has been conducted to address necessary topics such as the estimation and use of error covariance [3], [4], [6], [7], most methods of navigation using laser scanners are ad hoc, with minimal analysis of the confidence, accuracy, integrity, or integration of the solution with other sensors. While most existing approaches are only loosely coupled with odometry, an integration of 2D laser scans with the Global Positioning System (GPS) in the range-domain (generally referred to as tight coupling) is reported in [8].

3.0 2D NAVIGATION MECHANIZATION

3.1 Generic Approach

As mentioned in the Introduction section, features extracted from 2D laser scan images are used to navigate. Lines are employed for the feature representation. Line-based navigation was selected for the following reasons:

- Lines are common in man-made environments. For instance, building walls can be generally approximated as planar surfaces. An intersection of a laser scanning plane with a planar surface creates a line in the scan image.
- Lines are highly repeatable in multiple scans. If a wall of a building stays in the scanner measurement range then the lines associated with that wall repeat in the scan images.
- Computationally efficient procedures exist to extract lines from scan images [9].

Line-based navigation is performed utilizing three consecutive steps as given below:

- A modified incremental split and merge algorithm described in the next subsection is applied to extract lines from scan images.
- Extracted lines are matched with coinciding lines from previous scans (see the Line Matching subsection below).
- Changes in line parameters are applied to compute a relative navigation solution: namely changes in position and heading (see the Derivation of Relative Navigation Solution subsection below).

Essentially, line-based navigation is performed using a normal point of a line where the normal point is defined by the perpendicular intersection of the extracted line and a line originating from the laser scanner. Figure 4 illustrates a line normal point.

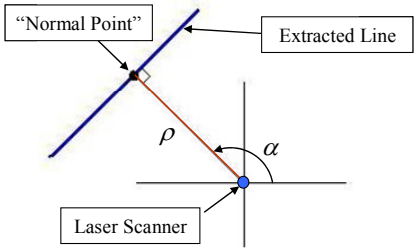

Figure 4: Line Representation using the Normal Point

A normal point is characterized by its polar parameters: range and angle. The change in the perceived location of this point between scans is used to estimate the change in position and heading of the laser.

3.2 Line Extraction Routine

A significant amount of research has been conducted towards the extraction of lines from laser scans and a number of methods have been published [2], [9]. The method applied in this paper is called the Modified Incremental Split and Merge (MISM) algorithm. As the name implies, this method is a combination of the Split and Merge and Incremental methods found in [2] and [9] with a few other modifications.

The MISM line extraction algorithm starts with the first two points of the scan and creates a line from these points. The line is created by solving for polar line parameters (ρ,α). These parameters are defined by applying Least Mean Square (LMS) line estimation [2] formulated by Equation 1:

$$\bar{x} = \frac{1}{N}\sum_{n=1}^{P} x_n, \quad \bar{y} = \frac{1}{N}\sum_{n=1}^{N} y_n$$

$$\alpha = \frac{1}{2}\arctan\left(\frac{-2\cdot\sum_{n=1}^{N}(\bar{x}-x_n)\cdot(\bar{y}-y_n)}{\sum_{n=1}^{N}(\bar{y}-y_n)^2 - \sum_{n=1}^{N}(\bar{x}-x_n)^2}\right) \qquad \text{Eq. 1}$$

$$\rho = \bar{x}\cdot\cos(\alpha) + \bar{y}\cdot\sin(\alpha)$$

$$\sigma_{line} = \mathrm{std}(\rho - x_n\cos(\alpha) - y_n\sin(\alpha))$$

where $(x_n)_{n=1}^{N}$ and $(y_n)_{n=1}^{N}$ are Cartesian coordinates of the points applied for the LMS line fit, and σ_{line} is the standard deviation of the distance of the points to the line.

Subsequent scan points are added to the line one by one and the polar parameters and standard deviation are recalculated after the addition of each point. The process repeats until either a point is found with a Euclidian distance from the line that is greater than a predefined distance threshold or the standard deviation of the line with the point added exceeds a predefined standard deviation threshold. The Euclidian distance d_n of the point ((x_n, y_n)) to the line is found using the equation for shortest distance to a line [2]:

$$d_n = \rho - x_n\cdot\cos(\alpha) - y_n\cdot\sin(\alpha) \qquad \text{Eq. 2}$$

The allowable threshold for the point's Euclidian distance to the line is found using a multiple of the expected range error standard deviation given by:

$$d_n \le \gamma\cdot\sigma_r \qquad \text{Eq. 3}$$

where γ is typically set between 1 and 5, a value that is set based upon desired performance, and is calculated using error covariance calculations found in [6] or by simply using the rated standard deviation of the scanning laser. By multiplying the variance by a constant, the physical line's texture and moderate statistical outliers are taken into consideration.

The allowable threshold for the line standard deviation is set to:

$$\sigma_{line} \leq \kappa \cdot \sigma_{line\_expected} \qquad \text{Eq. 4}$$

where κ is typically set between 1 and 5 based upon desired performance. The expected line variance $\sigma_{line\_expected}$ is either calculated using expected line covariance calculations found in [6] or by simply using the rated standard deviation of the scanning laser. This value is multiplied by a constant to take into account both imperfections in the physical line and moderate outliers. Once a point is added that causes one of the two conditions to fail, the previously added points are stored as a line and the new point is stored as the first point of the next line.

When all lines have been found, an extensive search is conducted to find lines that can be merged. This merging operation is performed by combining the points of two lines together and solving for the resulting polar parameters and standard deviation. If the standard deviation of the merged lines is lower than the threshold given in Equation 4, the two lines are stored as a new merged line, which is in turn stored for further merging. The merging process is performed for all possible combinations of the extracted lines. Merging of lines with similar parameters generally reduces the number of lines, helping greatly during the line matching step. Figure 5 shows the results of the MISM algorithm for a set of real outdoor data.

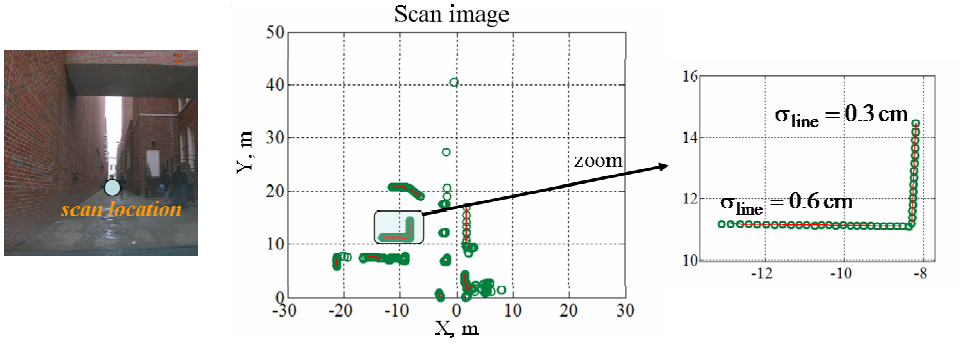

Figure 5: Results of Modified Split and Merge Line Extraction

3.3 Derivation of Relative Navigation Solution

This subsection discusses the derivation of a 2D relative position and heading solution from changes in line parameters. As mentioned previously, changes in perceived locations of line normal points are applied to compute a relative navigation solution. Figure 6 illustrates changes in parameters of a line normal point created by user motion between scans i and j.

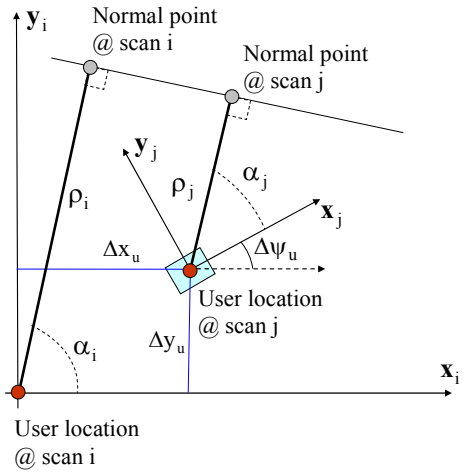

Figure 6: Changes in Line Parameters due to User Motion

Figure 6 uses the following notation:

$(\mathbf{x}_i, \mathbf{y}_i)$ are axes of the i-scan frame, which is the laser scanner body frame at scan i;

$(\mathbf{x}_j, \mathbf{y}_j)$ are axes of the j-scan frame;

ρ_i is the normal point polar range at scan i;

ρ_j is the normal point polar range at scan j;

α_i is the normal point polar angle at scan i;

α_j is the normal point polar angle at scan j;

$\Delta\mathbf{R}_u = \begin{bmatrix} \Delta x_u \\ \Delta y_u \end{bmatrix}$ is the vector of user displacement between scans i and j;

$\Delta\psi_u$ is the change in user heading angle between scans i and j.

Equation 5 employs polar parameters of the line normal point to formulate a line equation that is expressed at the i-scan frame [2]:

$$x \cdot \cos(\alpha_i) + y \cdot \sin(\alpha_i) = \rho_i \qquad \text{Eq. 5}$$

where (x, y) is the Cartesian coordinate pair of a point that belongs to the line.

Euclidian distance from the line to a point with a Cartesian coordinate pair (x_0, y_0) at the i-scan frame is determined using Equation 6:

$$d_0 = \rho_i - x_0 \cdot \cos(\alpha_i) - y_0 \cdot \sin(\alpha_i) \qquad \text{Eq. 6}$$

According to Figure 1, the user location point at scan j has coordinates $(\Delta x_u, \Delta y_u)$ at the i-scan frame. The distance from this point to the line equals ρ_j. Correspondingly, substituting (x_0, y_0) by $(\Delta x_u, \Delta y_u)$ and d_0 by ρ_j in Equation 6 yields:

$$\rho_j = \rho_i - \Delta x_u \cdot \cos(\alpha_i) - \Delta y_u \cdot \sin(\alpha_i) \qquad \text{Eq. 7}$$

or:

$$\Delta x_u \cdot \cos(\alpha_i) + \Delta y_u \cdot \sin(\alpha_i) = \rho_i - \rho_j \qquad \text{Eq. 8}$$

Equation 8 represents a linear relation for the estimation of components of the position change vector between scans i and j. For cases where multiple lines are extracted from scans i and j, the position change vector can be estimated through a weighted LMS solution routine:

$$\Delta \mathbf{R}_u = \left(\mathbf{H}_{\Delta \mathbf{R}}^T \cdot \mathbf{W} \cdot \mathbf{H}_{\Delta \mathbf{R}}\right)^{-1} \cdot \left(\mathbf{H}_{\Delta \mathbf{R}}^T \cdot \mathbf{W} \cdot \mathbf{Y}_{\Delta \mathbf{R}}\right) \qquad \text{Eq. 9}$$

where:

$\mathbf{H}_{\Delta \mathbf{R}}$ is the observation matrix;

$\mathbf{Y}_{\Delta \mathbf{R}}$ is the measurement matrix;

$\mathbf{W}$ is the weight matrix.

The matrices above are formulated as follows. The observation matrix is given by Equation 10:

$$\mathbf{H}_{\Delta \mathbf{R}} = \begin{bmatrix} \cos(\alpha_{i,(1)}) & \sin(\alpha_{i,(1)} \\ \cdots & \\ \cos(\alpha_{i,(n)}) & \sin(\alpha_{i,(n)}) \end{bmatrix} \qquad \text{Eq. 10}$$

where index i,(k) denotes a kth line extracted from a scan image at scan i. Equation 11 defines the measurement matrix:

$$\mathbf{Y}_{\Delta\mathbf{R}} = \begin{bmatrix} \rho_{i,(1)} - \rho_{j,(1)} \\ \dots \\ \rho_{i,(n)} - \rho_{j,(n)} \end{bmatrix} \qquad \text{Eq. 11}$$

where index j,(k) denotes a kth line extracted from a scan image at scan j. It is assumed herein that lines are matched between scans i and j; i.e. indexes i,(k) and j,(k) represent the same line that is being extracted from scans i and j, correspondingly. Details of the line matching routine are discussed in the next subsection. The weight matrix is provided by Equation 12:

$$\mathbf{W} = \begin{bmatrix} w_{(1)} & 0 & \vdots & 0 & \\ 0 & w_{(2)} & & & \\ \cdots & & \cdots & \cdots & \\ & & & w_{(n-1)} & 0 \\ 0 & & \vdots & 0 & w_{(n)} \end{bmatrix} \qquad \text{Eq. 12}$$

where $w_{(k)}, k = 1,...,n$ are weights assigned to lines extracted from scan images.

Weights for the LMS solution are generally assigned based on measurement quality. The solution procedure developed herein thus applies line standard deviations to perform the weight assignment:

$$w_{(k)} = \frac{1}{\sigma^2_{i,(k)} + \sigma^2_{j,(k)}}, k = 1,...,n \qquad \text{Eq. 13}$$

where $\sigma^2_{i,(k)}, k = 1,...,n$ and $\sigma^2_{j,(k)}, k = 1,...,n$ are line standard deviations for scan images i and j, correspondingly. Standard deviation values are computed by the MISM algorithm discussed above.

It is important to mention that transformation of line extraction errors into position errors is determined by the relative line geometry. The error transformation coefficient is minimized for those cases where perpendicular lines are extracted. The position solution is singular if all of the lines extracted are parallel to each other.

From the geometry presented in Figure 6, the change in the user heading angle and change in the line polar angle are related as follows:

$$\Delta\psi_u = \alpha_i - \alpha_j \qquad \text{Eq. 14}$$

Similarly to the estimation of the position change vector, a weighted LMS solution is applied to estimate changes in heading angle for cases where multiple lines are extracted:

$$\Delta\psi_u = \left(\mathbf{H}^T_{\Delta\psi} \cdot \mathbf{W} \cdot \mathbf{H}_{\Delta\psi}\right)^{-1} \cdot \left(\mathbf{H}^T_{\Delta\psi} \cdot \mathbf{W} \cdot \mathbf{Y}_{\Delta\psi}\right) \qquad \text{Eq. 15}$$

where:

$$\mathbf{H}_{\Delta\psi} = \begin{bmatrix} 1 \\ 1 \\ \cdots \\ 1 \end{bmatrix} \qquad \text{Eq. 16}$$

$$\mathbf{Y}_{\Delta\psi} = \begin{bmatrix} \alpha_{i,(1)} - \alpha_{j,(1)} \\ \alpha_{i,(2)} - \alpha_{j,(2)} \\ \cdots \\ \alpha_{i,(n)} - \alpha_{j,(n)} \end{bmatrix} \qquad \text{Eq. 17}$$

From Equation 16 it can be inferred that the observation matrix $\mathbf{H}_{\Delta\psi}$ does not depend on line geometry. The estimation of relative heading angle is therefore geometry independent. No singular cases exist for the heading angle estimation.

3.4 Line Matching

As formulated above, the relative navigation solution is found by using the perceived change in the navigational objects (lines) from one scan to the next. In order to analyze the position and orientation change of a line from one scan to the next, the line must be found in both scans and it must be known with certainty that a line in one scan corresponds to a line in the next scan. This is done by predicting where a line normal point will be located in the next scan and opening a search window around this point to allow for uncertainties.

Figure 2 illustrates the line matching procedure. User position and orientation at the current scan (scan j in Figure 7) are first predicted using INS outputs that include a 2D displacement vector $\Delta\mathbf{R}_{INS}$ and a heading increment $\Delta\psi_{INS}$. Next, polar parameters of the normal point extracted from the previous scan (scan i in Figure 7) and predicted user position and orientation are employed to predict the location of the normal point at the current scan.

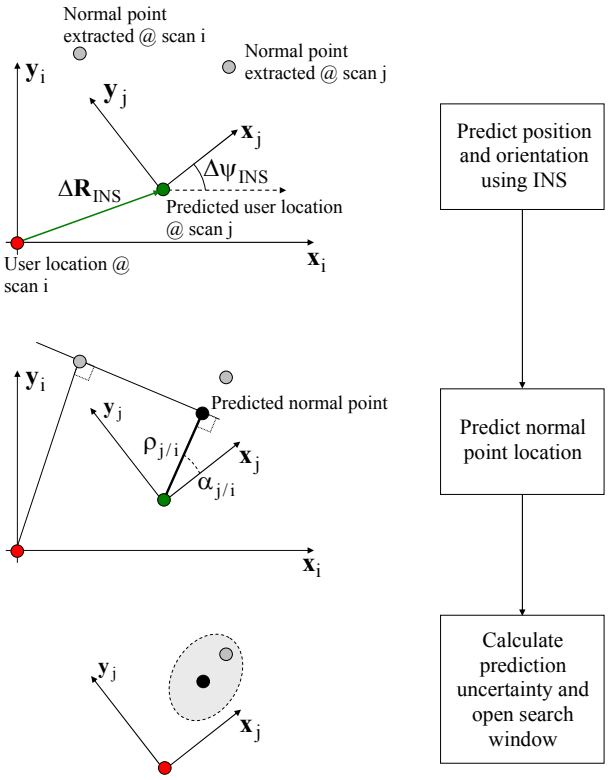

Figure 7: Line Matching

Prediction computations herein are derived from Equation 7 and Equation 14:

$$\rho_{j/i} = \rho_i - \Delta x_{INS} \cdot \cos(\alpha_i) - \Delta y_{INS} \cdot \sin(\alpha_i)$$
$$\alpha_{j/i} = \alpha_i - \Delta\psi_{INS} \qquad \text{Eq. 18}$$

where:

$\rho_{j/i}$ is the predicted polar range of the normal point at the current scan;

$\alpha_{j/i}$ is the predicted polar angle of the normal point at the current scan.

Prediction uncertainty is then evaluated. Particularly, a prediction covariance matrix is computed as follows:

$$\mathbf{cov}_{\delta\rho_{j/i},\delta\alpha_{j/i}} = \mathbf{cov}_{\delta\rho_i,\delta\alpha_i} + \left(\mathbf{cov}_{\delta\rho,\delta\alpha}\right)_{INS} \qquad \text{Eq. 19}$$

where:

$\mathbf{cov}_{\delta\rho_{j/i},\delta\alpha_{j/i}}$ is the prediction covariance;

$\mathbf{cov}_{\delta\rho_i,\delta\alpha_i}$ is the covariance of the line extracted from the previous scan;

$\left(\mathbf{cov}_{\delta\rho,\delta\alpha}\right)_{\text{INS}}$ is the prediction covariance component that is due to inertial errors.

A simplified expression that assumes uncorrelated range and angular errors ($\delta\rho_i$ and $\delta\alpha_i$) is applied to compute the line error covariance for the implementation considered in this paper:

$$\mathbf{cov}_{\delta\rho_i,\delta\alpha_i} = \begin{bmatrix} \sigma^2_{\delta\rho_i} & 0 \\ 0 & \sigma^2_{\delta\alpha_i} \end{bmatrix} \qquad \text{Eq. 20}$$

Line standard deviations computed by the MISM extraction algorithm (see Equation 1) are used to evaluate the range variance:

$$\sigma^2_{\delta\rho_i} = \sigma^2_{\text{line}} \qquad \text{Eq. 21}$$

It is important to mention that the line variance computation formulated by Equation 1 uses actual noise samples of a line to compute its variance, where line noise is comprised of laser measurement errors and a texture of a scanned surface.

A fixed-value uncertainty chosen a priori is applied for the angular variance computation:

$$\sigma^2_{\delta\alpha_i} = \delta\alpha^2_0 \qquad \text{Eq. 22}$$

where $\delta\alpha_0 = 2\,\text{deg}$ is currently used.

Reference [6] takes into account correlation between range and angular errors and computes the line covariance matrix for the case where laser measurement errors only are considered. Future research will address computation of the line error covariance for a general case that accounts for: a) correlation between range and angular errors; b) both laser measurement errors and texture-induced errors.

Equation 23 provides INS covariance computations:

$$\left(\mathbf{cov}_{\delta\rho,\delta\alpha}\right)_{\text{INS}} = \mathbf{H}_{\text{INS}} \cdot \mathbf{P}_{\text{INS}} \cdot \mathbf{H}^{\text{T}}_{\text{INS}} \qquad \text{Eq. 23}$$

where:

$\mathbf{P}_{\text{INS}}$ is the inertial error covariance matrix. This matrix is estimated by the Kalman filter that performs calibration of INS error states (see the Tight Coupling of Laser Scanner and Inertial Data section below);

$\mathbf{H}_{INS}$ is the inertial observation matrix that transforms inertial error states into line range error and line angular error.

Equation 24 exemplifies the $\mathbf{H}_{INS}$ matrix for the case where a seven-state model is used to characterize inertial errors and particular error states include two horizontal position change states, two horizontal velocity states, and three angular states (pitch, roll, and heading errors):

$$\mathbf{H}_{INS} = \begin{bmatrix} -\cos(\alpha_i) & -\sin(\alpha_i) & 0 & 0 & 0 & 0 & -1 \end{bmatrix} \quad \text{Eq. 24}$$

Following the prediction covariance computation, a search window is opened to accommodate the prediction uncertainty. A certain threshold criterion needs to be applied to construct the search window. Example criteria include an independent range and angle test and a Chi-squared test. A search window for the independent range and angle test criterion is formulated by Equation 25:

$$\begin{aligned} &(\rho_{j/i} - \rho_j)^2 < K_\rho \cdot \left(\mathbf{cov}_{\delta\rho_{j/i},\delta\alpha_{j/i}}\right)_{11} \\ &\text{and} \qquad \text{Eq. 25} \\ &(\alpha_{j/i} - \alpha_j)^2 < K_\alpha \cdot \left(\mathbf{cov}_{\delta\rho_{j/i},\delta\alpha_{j/i}}\right)_{22} \end{aligned}$$

where:

K_ρ and K_α are predetermined test scale factors;

$\left(\mathrm{cov}_{\delta\rho_{j/i},\delta\alpha_{j/i}}\right)_{pl}$ is the element of the covariance matrix that belongs to the pth row and lth column.

Equation 26 defines the search window for a case where a Chi-squared test is applied:

$$\begin{bmatrix} \rho_{j/i} - \rho_j & \alpha_{j/i} - \alpha_j \end{bmatrix} \cdot \left(\mathbf{cov}_{\delta\rho_{j/i},\delta\alpha_{j/i}}\right)^{-1} \cdot \begin{bmatrix} \rho_{j/i} - \rho_j \\ \alpha_{j/i} - \alpha_j \end{bmatrix} < 2 \quad \text{Eq. 26}$$

As mentioned previously, line covariance computations currently applied assume independent range and angular line errors. The independent range and angle test criterion is thus employed for line matching. Future developments will address the use of the Chi-squared search criterion that takes into account correlation of range and angular errors.

A line match search is the final step of the matching procedure. If a normal point extracted from the current scan (scan j in Figure 7) fits within the search window then a match is declared. For those cases where multiple matches exist, a line with normal point that has a minimum distance to the predicted normal point location is chosen.

4.0 EXTENSION INTO A PARTIAL 3D CASE: COMPENSATION OF LASER SCANNER TILT

The 2D navigation mechanization considered in the previous section does not take into account the fact that a laser scan plane can tilt from scan to scan. In other words, it is assumed that the laser always scans in the same plane. This assumption is generally invalid for practical application cases; e.g. if the laser is mounted on a vehicle that is driving through a city street then the laser scan plane can have different tilt angles at different scans. Figure 8 illustrates the influence of laser scanner tilt on the estimation of line parameters.

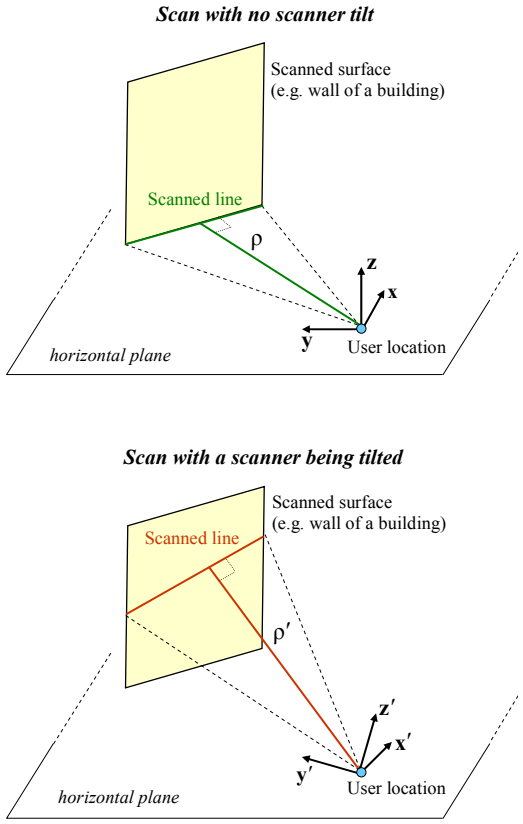

Figure 8: Influence of Laser Scanner Tilt on Line Parameter Estimation

Accordingly, the laser first scans in the horizontal plane. Intersection of the horizontal scanning beam with a planar surface (e.g. a wall of building) creates a line in the scan image. Next, a tilted scan is considered where the original laser body frame $(\mathbf{x},\mathbf{y},\mathbf{z})$ is tilted into the $(\mathbf{x}',\mathbf{y}',\mathbf{z}')$ frame. A line with changed line parameters is observed in the scan image. For instance, a polar range ρ' of the line normal point for the tilted scan differs from the normal point polar range ρ for the horizontal scan as illustrated in Figure 8. Changes in line parameters that are due to uncompensated laser scanner tilt introduce navigation errors. A tilt compensation procedure was therefore developed.

The tilt compensation procedure developed uses estimates of platform tilt angles (pitch and roll) provided by the INS to computationally rotate a tilted scan image into a horizontal scan frame. The computational rotation is derived by first considering intersections of a planar surface with horizontal and tilted scan planes. Parameters of horizontal and tilted intersection lines are then related. Finally, a procedure for estimating parameters of horizontal intersection based on parameters of tilted intersection is developed. A line of intersection of a planar surface with a horizontal scan plane is thus reconstructed from line parameters extracted from a tilted scan image. This reconstruction essentially rotates a tilted scan image into a horizontal scan frame. Steps for the derivation of the rotation procedure are discussed below.

Equation 27 provides a general equation of a planar surface in three dimensions:

$$x \cdot \cos(\alpha) \cdot \cos(\theta) + y \cdot \sin(\alpha) \cdot \cos(\theta) + z \cdot \sin(\theta) = \rho \qquad \text{Eq. 27}$$

Vertical planes for which $\theta = 0$ are assumed herein. The vertical plane assumption is applied since indoor and outdoor urban environments are considered where most of the planar surfaces are created by building walls that can be assumed vertical. Accordingly, a vertical plane equation at the $(\mathbf{x},\mathbf{y},\mathbf{z})$ frame has the following form:

$$x \cdot \cos(\alpha) + y \cdot \sin(\alpha) = \rho \qquad \text{Eq. 28}$$

Intersection of a planar surface with a horizontal scan plane $(\mathbf{x},\mathbf{y})$ is derived by setting z=0. Since z is absent in the plane formulation, Equation 28, the intersection line equation is defined by Equation 28. Therefore, ρ and α represent polar parameters of the normal point in the non-tilted scan frame $(\mathbf{x},\mathbf{y})$.

A plane equation is expressed in the tilted frame $(\mathbf{x}',\mathbf{y}',\mathbf{z}')$ in order to derive the intersection line equation for the tilted scan frame. A coordinate transformation from tilted $(\mathbf{x}',\mathbf{y}',\mathbf{z}')$ to the non-tilted frame $(\mathbf{x},\mathbf{y},\mathbf{z})$ is defined as follows:

$$\begin{bmatrix} x \\ y \\ z \end{bmatrix} = \mathbf{C} \cdot \begin{bmatrix} x' \\ y' \\ z' \end{bmatrix} \qquad \text{Eq. 29}$$

where $\mathbf{C} = \mathbf{C}^{(\mathbf{x},\mathbf{y},\mathbf{z})}_{(\mathbf{x}',\mathbf{y}',\mathbf{z}')}$ is the coordinate transformation matrix from the tilted frame $(\mathbf{x}',\mathbf{y}',\mathbf{z}')$ to the non-tilted frame $(\mathbf{x},\mathbf{y},\mathbf{z})$. The coordinate transformation matrix is derived from inertial data. Particularly, the relative navigation frame (N-frame) is used as a non-tilted frame for the implementation considered in this paper. A tilted frame is represented by the current scan frame, which is the same as the platform body frame (b-frame). The matrix $\mathbf{C}$ thus corresponds to a body/navigation frame direction cosine matrix $\mathbf{C}^{N}_{b}$. The direction cosine matrix $\mathbf{C}^{N}_{b}$ is commonly used by inertial systems to characterize the attitude and is computed by integrating inertial gyro outputs [10].

Performing matrix multiplications in Equation 29 yields:

$$\begin{aligned} x &= C_{11} \cdot x' + C_{12} \cdot y' + C_{13} \cdot z' \\ y &= C_{21} \cdot x' + C_{22} \cdot y' + C_{23} \cdot z' \end{aligned} \qquad \text{Eq. 30}$$

Substitution of Equation 30 into Equation 28 gives the following:

$$\begin{aligned} &\left(C_{11} \cdot x' + C_{12} \cdot y' + C_{13} \cdot z'\right) \cdot \cos(\alpha) + \\ &\left(C_{21} \cdot x' + C_{22} \cdot y' + C_{23} \cdot z'\right) \cdot \sin(\alpha) = \rho \end{aligned} \qquad \text{Eq. 31}$$

or

$$\begin{aligned} &x' \cdot \left(C_{11} \cdot \cos(\alpha) + C_{21} \cdot \sin(\alpha)\right) + \\ &y' \cdot \left(C_{12} \cdot \cos(\alpha) + C_{22} \cdot \sin(\alpha)\right) + \\ &z' \cdot \left(C_{13} \cdot \cos(\alpha) + C_{23} \cdot \sin(\alpha)\right) = \rho \end{aligned} \qquad \text{Eq. 32}$$

Equation 32 provides the equation of the vertical planar surface represented in the tilted coordinate frame. This surface intersects with the tilted scan plane $(\mathbf{x}', \mathbf{y}')$ at $z' = 0$. The intersection line equation is thus expressed as follows:

$$\begin{aligned} &x' \cdot \left(C_{11} \cdot \cos(\alpha) + C_{21} \cdot \sin(\alpha)\right) + \\ &y' \cdot \left(C_{12} \cdot \cos(\alpha) + C_{22} \cdot \sin(\alpha)\right) = \rho \end{aligned} \qquad \text{Eq. 33}$$

When the same line is extracted from the tilted scan image it has the following representation:

$$x' \cdot \cos(\alpha') + y' \cdot \sin(\alpha') = \rho' \qquad \text{Eq. 34}$$

where ρ' and α' are parameters of the intersection line normal point in the tilted frame.

Note that Equations 33 and 34 express the same line using parameters of the normal points for line intersections with horizontal and tilted scan planes, correspondingly. These equations can be thus applied to relate normal point parameters in horizontal and tilted scan images. Using Equation 33:

$$y' = 0 \Rightarrow x' = \frac{\rho}{\left(C_{11} \cdot \cos(\alpha) + C_{21} \cdot \sin(\alpha)\right)} \qquad \text{Eq. 35}$$

Similarly for Equation 34:

$$y' = 0 \Rightarrow x' = \frac{\rho'}{\cos(\alpha')} \qquad \text{Eq. 36}$$

Comparison of Equations 35 and 36 provides:

$$\frac{\rho}{\left(C_{11}\cdot\cos(\alpha)+C_{21}\cdot\sin(\alpha)\right)}=\frac{\rho'}{\cos(\alpha')} \qquad \text{Eq. 37}$$

or:

$$\rho'\cdot\left(C_{11}\cdot\cos(\alpha)+C_{21}\cdot\sin(\alpha)\right)-\rho\cdot\cos(\alpha')=0 \qquad \text{Eq. 38}$$

Similar considerations can be performed by analyzing Equations 33 and 34 at $x'=0$. The following expression is derived for this case:

$$\rho'\cdot\left(C_{12}\cdot\cos(\alpha)+C_{22}\cdot\sin(\alpha)\right)-\rho\cdot\sin(\alpha')=0 \qquad \text{Eq. 39}$$

Equations 38 and 39 determine a system of non-linear equations for the estimation of range and angle that are the normal point parameters in the horizontal scan frame. This system is solved iteratively by applying linearizations. The system is linearized around the previous estimates of range and angle for each iteration. Adjustments to the previous estimates are then computed through the solution of linear equation systems. To start iterations, initial estimates are obtained as follows:

$$\begin{gathered}\hat{\rho}=\rho' \\ \begin{bmatrix}\cos(\hat{\alpha})\\ \sin(\hat{\alpha})\end{bmatrix}=\begin{bmatrix}C_{11} & C_{21}\\ C_{12} & C_{22}\end{bmatrix}^{-1}\cdot\begin{bmatrix}\cos(\alpha')\\ \sin(\alpha')\end{bmatrix} \\ \hat{\alpha}=\arctan(\sin(\hat{\alpha}),\cos(\hat{\alpha}))\end{gathered} \qquad \text{Eq. 40}$$

where $\arctan(.,.)$ is a 4-quadrant arctangent function illustrated by Figure 9.

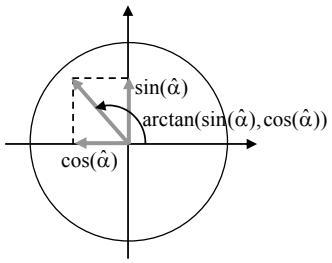

Figure 9: Four-Quadrant Arctangent Function

Determining parameters of the normal point in the horizontal frame by iteratively solving the non-linear equation system (Equations 38 and 39) essentially rotates tilted scan image into a horizontal frame. The tilt compensation applied allows for an extension of the 2D navigation case by removing constrains on the laser angular motion.

5.0 TIGHT COUPLING OF LASER SCANNER AND INERTIAL DATA

Figure 10 illustrates the structure of a tightly coupled laser scanner/inertial integrated navigation. As discussed previously, inertial data are applied to predict line parameters between scans and to compensate for a tilt of the laser scanner platform. Laser images are used for the in-motion calibration of inertial error states in order to reduce drift of INS navigation outputs. The INS calibration part and laser-based position computations are separated. A dynamic state range-domain INS calibration is applied herein. Since the INS is calibrated in the laser measurement domain, the integration mechanization is considered tightly coupled. Similar to the case of GPS/INS integration, one of the main advantages of tight coupling over a loosely coupled position-domain INS calibration is the ability to reduce inertial drift for those cases where scan images do not contain enough features to compute a laser-based position. According to Figure 10, the relative position solution is computed based on laser data with inertial coasting being employed for those cases where not enough features are extracted from scan images to compute a laser-based relative position.

The dynamic-state INS calibration uses a Kalman filter to periodically estimate inertial error states. The estimation process is based on a complementary Kalman filter methodology [11], which employs differences between INS and laser scanner observables as filter measurements. Changes in polar ranges of line normal points between consecutive scans are used as laser observables. Correspondingly, laser scanner observables of the Kalman filter are formulated as follows for scan m:

$$\left(\Delta\boldsymbol{\rho}_{\mathrm{LS}}\right)_{\mathrm{m}} = \begin{bmatrix} \rho_{\mathrm{m-1},(1)} - \rho_{\mathrm{m},(1)} \\ \cdots \\ \rho_{\mathrm{m-1},(\mathrm{n})} - \rho_{\mathrm{m},(\mathrm{n})} \end{bmatrix} \qquad \text{Eq. 41}$$

where n is the number of lines that are matched between scans m and m-1. Inertial observables use the INS displacement vector that is transformed into the range domain as follows:

$$\left(\Delta\boldsymbol{\rho}_{\mathrm{INS}}\right)_{\mathrm{m}} = \left(\mathbf{H}_{\Delta\mathbf{R}}\right)_{\mathrm{m-1}} \cdot \left(\left(\Delta\mathbf{R}_{\mathrm{INS}}\right)_{\mathrm{m}} + \left(\Delta\mathbf{C}_{\mathrm{b}}^{\mathrm{N}}\right)_{\mathrm{m}} \cdot \boldsymbol{L}_{\mathrm{b}}\right) \qquad \text{Eq. 42}$$

where:

$\left(\mathbf{H}_{\Delta\mathbf{R}}\right)_{\mathrm{m-1}}$ is computed from Equation 10 for i=m-1;

$\left(\Delta\mathbf{R}_{\mathrm{INS}}\right)_{\mathrm{m}}$ is the INS displacement vector between scans m and m-1;

$\left(\Delta\mathbf{C}_{\mathrm{b}}^{\mathrm{N}}\right)_{\mathrm{m}} = \left(\mathbf{C}_{\mathrm{b}}^{\mathrm{N}}\right)_{\mathrm{m}} - \left(\mathbf{C}_{\mathrm{b}}^{\mathrm{N}}\right)_{\mathrm{m-1}}$

$\boldsymbol{L}_{\mathrm{b}}$ is the lever arm vector pointed from the INS to the laser scanner with the vector components given at the laser scanner-defined body frame.

As mentioned previously, filter measurements are defined as differences between inertial and laser scanner observables:

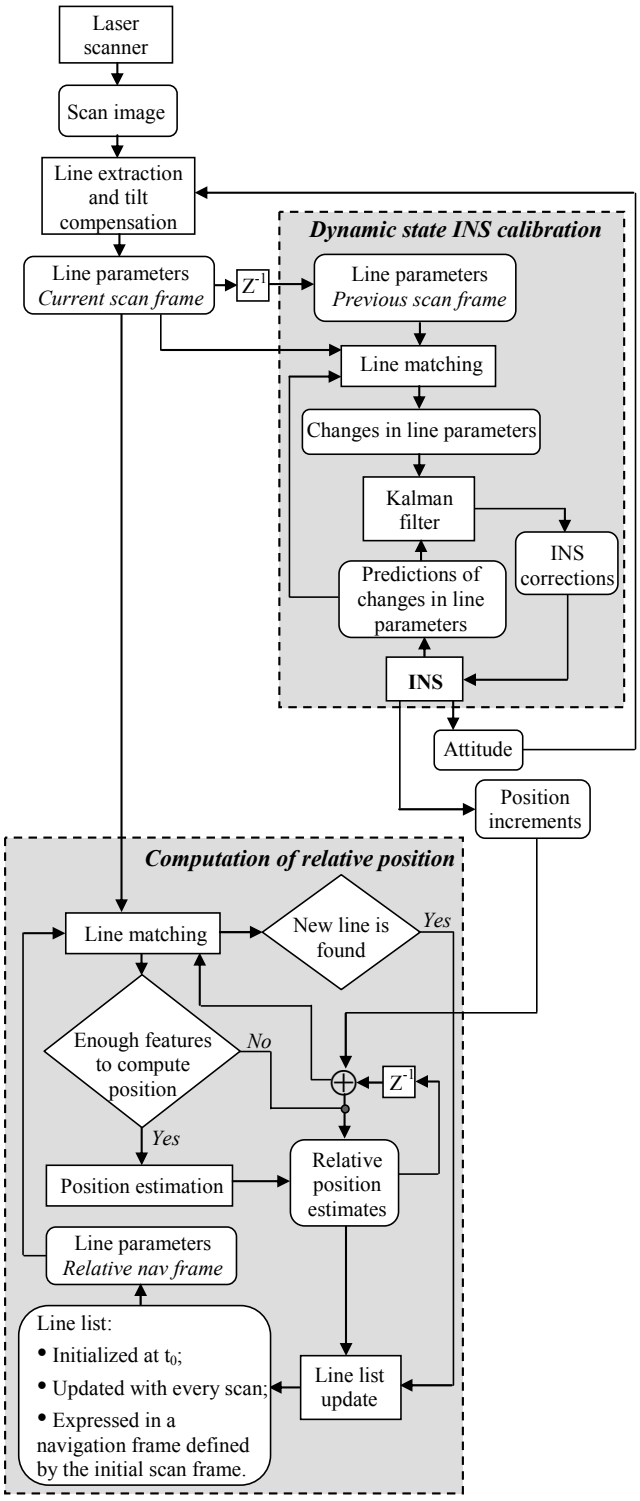

Figure 10: Structure of Tightly-Coupled Laser Scanner/Inertial Navigation Solution

$$\left(\mathbf{Y}_{\text{Kalman}}\right)_{\text{m}} = \left(\Delta\boldsymbol{\rho}_{\text{INS}}\right)_{\text{m}} - \left(\Delta\boldsymbol{\rho}_{\text{LS}}\right)_{\text{m}} \qquad \text{Eq. 43}$$

The filter operates with dynamic states only (position error states are not used). Particular filter states include: errors in position changes between consecutive scans (2 states); velocity errors (2 states); attitude errors (3 states); gyro biases (3 states); accelerometer biases (3 states). Equation 44 defines the filter observation matrix $\mathbf{H}_{\text{Kalman}}$:

$$\left(\mathbf{H}_{\text{Kalman}}\right)_{\text{m}} = \begin{bmatrix} \cos(\alpha_{\text{m-1,(1)}}) & \sin(\alpha_{\text{m-1,(1)}}) & 0 & \dots & 0 \\ & \dots & & & \\ \cos(\alpha_{\text{m-1,(n)}}) & \sin(\alpha_{\text{m-1,(n)}}) & 0 & \dots & \end{bmatrix} \qquad \text{Eq. 44}$$

The measurement noise matrix $\mathbf{R}_{\text{Kalman}}$ is given by Equation 45:

$$\left(\mathbf{R}_{\text{Kalman}}\right)_{\text{m}} = \left(\mathbf{W}_{\text{m,m-1}}\right)^{-1} \qquad \text{Eq. 45}$$

where $\mathbf{W}_{\text{m,m-1}}$ is computed from Equations 12 and 13 using i=m-1 and j=m.

Derivation of the filter state transition matrix and the system noise matrix for the filter states chosen employs a standard Kalman filter formulation, which can be found in [11]. With the filter states listed above, filter measurements defined by Equations 41 through 43, and filter matrices defined by Equations 44 and 45, the INS calibration procedure implements a complementary Kalman filter algorithm for the estimation of the inertial error states. The filter algorithm is well-documented and can be found in [11]. Note that the Kalman filter implementation considered herein does not take into account a correlation between errors in estimated ranges of extracted line normal points and inertial attitude errors. This correlation is due to the use of inertial attitude for the compensation of laser scanner tilt. Accounting for the correlation between line range errors and inertial attitude errors is left for future developments.

As shown in Figure 10, the system relative position is computed separately from the INS calibration stage. Relative position is estimated based on lines extracted from the current scan image and a line list which contains lines from all the previous scans. The line list expresses line parameters in the relative navigation frame that is defined by the position and orientation of the laser scanner at the initial scan. The line list is initially populated at the initial scan. If a new line is seen at one of the following scans this line is added to the list with line parameters being transformed into the initial scan frame. The relative position is thus estimated based on changes in line parameters between the current scan frame and the initial scan frame. It is important to mention that addition of new lines to the line list generally improves the feature geometry and availability but at the same time creates a drift in the relative position solution. If the same lines are seen in the initial scan and the following scans then errors in the relative position estimate are due to line extraction errors in the current and initial scans only. For this case, the position solution does not drift. If a new line is seen, it is transformed into the initial frame using the current position estimate. Errors in the position estimate are thus transformed into errors in line parameters and add up to line extraction errors. As a result, the current position error contributes to the position error for the next scan where the new line is used for navigation. A position drift is thus created. This position drift is however generally significantly smaller as compared to the case where position increments are estimated based on consecutive scans thus introducing a random walk.

6.0 TEST RESULTS

This section uses results of live laser scanner and inertial data tests to demonstrate performance characteristics of the integrated laser/inertial solution developed. The following equipment was used throughout the test procedures implemented:

- Laser scanner: SICK LMS-200 [12]. A centimeter distance measurement mode was chosen. For this mode, a standard deviation of noise in laser range measurements is specified as 5 mm. The maximum measurement/detection range is 80 m. A scan angular range from 0 to 180 deg with an angular resolution of 0.5 deg was applied. A scanner update rate of approximately 0.7 scans/s was used.
- Inertial Measurement Unit (IMU): Systron Donner DQI [13]. This IMU represents a typical tactical-grade unit.
- GPS receiver (outdoor tests only): NovAtel OEM-4 receiver [14] connected to a NovAtel L1/L2 pinwheel antenna.
- Data synchronization board: Xilinx Spartan-3 Field Programmable Gate Arrays (FPGA) starter board [15]. The board decodes laser and inertial data from corresponding measurement sensors, time stamps the measurements decoded using the FPGA internal clock, and then sends synchronized measurements via a Digilent USB extension board [16] to a PC that collects the data for post-processing.
- Data processing: Post-processing implemented in Matlab™.

6.1 Indoor Test

Figure 11 shows a photograph of the indoor test setup. The equipment was mounted on a test cart that was manually pushed through hallways of the Ohio University Stocker Engineering Center. To create a reference trajectory, marks were put on the floor along the test path as illustrated by Figure 12. These marks were used as reference points. The cart was stopped at each reference point and the laser/inertial integrated readings were compared with reference point locations.

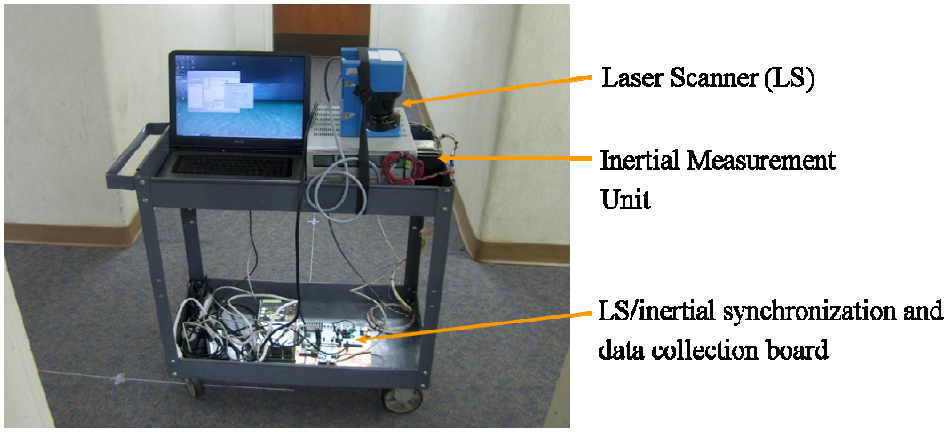

Figure 11: Indoor Test Setup

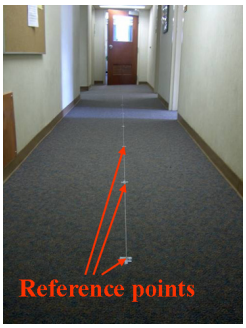

Figure 12: Reference Points for Indoor Test Trajectory

Figure 13 shows a test trajectory implemented for the indoor test case.

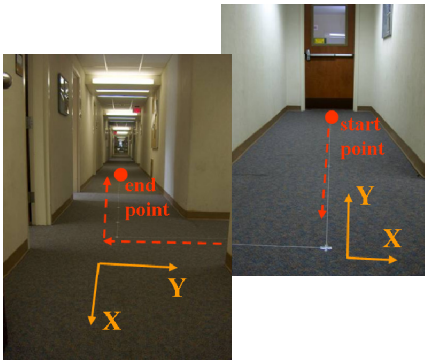

Figure 13: Indoor Test Scenario

It is important to note that the indoor test was designed to demonstrate potential of the laser/inertial integrated technology. The indoor test scenario implemented represents favorable conditions for the laser-based navigation. Particularly, good line geometry is generally available. Lines normally continue to stay in view of the laser scanner as the cart moves through hallways, which minimizes the drift in the position solution. Additionally, texture of indoor walls does not contribute significantly to line extraction errors. Outdoor tests considered in the next subsection represent significantly more challenges for the laser/inertial integrated solution.

Figure 14 compares the motion trajectory reconstructed from laser scanner and inertial measurements with reference points.

Errors in the laser/inertial solution are shown in Figure 15. Accordingly, relative position errors are limited to 10 cm after traveling a distance of 9 m (or 1.1% of distance traveled). A cm-accurate accurate trajectory reconstruction is thus demonstrated for the indoor test scenario considered.

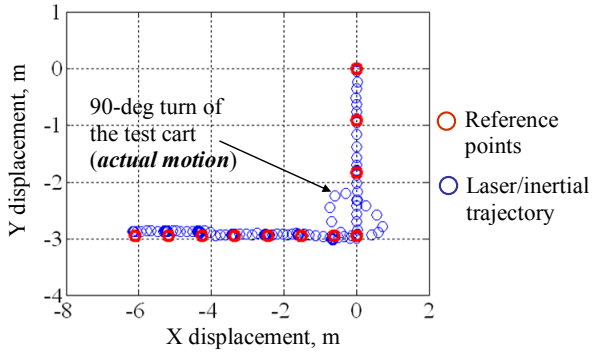

Figure 14: Indoor test: Reconstructed Test Trajectory

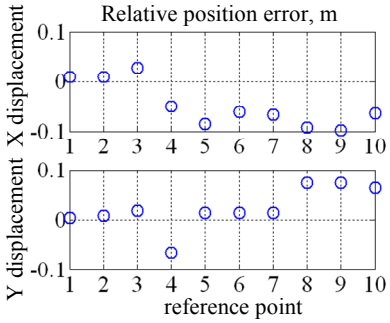

Figure 15: Indoor Test: Accuracy of Laser Scanner/Inertial Integrated Solution

Another way to characterize the trajectory accuracy is to use laser/inertial displacement residuals defined as:

$$\left(\delta\mathbf{R}_{\mathrm{LS/INS}}\right)_{\mathrm{m}} = \left(\Delta\mathbf{R}_{\mathrm{LS}}\right)_{\mathrm{m}} - \left(\Delta\mathbf{R}_{\mathrm{INS}}\right)_{\mathrm{m}} - \left(\Delta\mathbf{C}_{\mathrm{b}}^{\mathrm{N}}\right)_{\mathrm{m}} \cdot \boldsymbol{L}_{\mathrm{b}} \qquad \text{Eq. 46}$$

where $\left(\delta\mathbf{R}_{\mathrm{LS/INS}}\right)_{\mathrm{m}}$ is the laser-scanner based estimated position change that is computed from lines extracted for scan m and scan m-1 using weighted LMS computations defined by Equation 9.

Essentially, laser/inertial residuals characterize the level of noise in the reconstructed trajectory. Figure 16 provides residual plots for the indoor test case.

Residual standard deviations for the x and y displacement components herein are evaluated as follows:

$$\left(\sigma_{\delta\mathbf{R}_{\mathrm{LS/INS}}}\right)_{\mathrm{x}} = 2.0\ \mathrm{cm}$$
$$\left(\sigma_{\delta\mathbf{R}_{\mathrm{LS/INS}}}\right)_{\mathrm{y}} = 1.7\ \mathrm{cm}$$

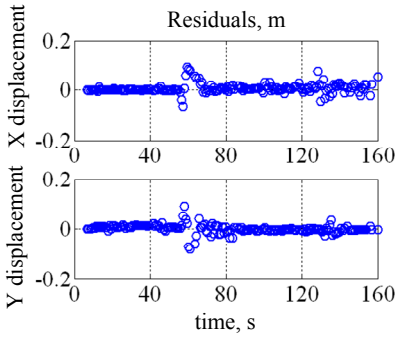

Figure 16: Indoor Test: Laser Scanner/Inertial Residuals

6.2 Outdoor Urban Test

A test van was used to collect data in urban streets of Athens, Ohio for the outdoor test. Figure 17 shows a photograph of the outdoor test setup.

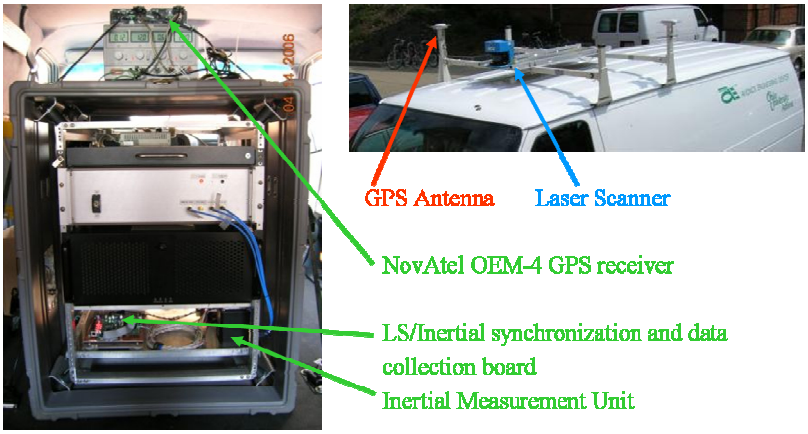

Figure 17: Outdoor Test Setup

A kinematic GPS position served as the only option for the absolute reference for outdoor test cases. The kinematic GPS solution was however mostly unavailable for the urban outdoor test trajectories. Kinematic GPS data were thus used to compute a total displacement only. To do so, the trajectory's start and end points were chosen in relatively open spots where enough GPS satellites were visible. Static GPS data collected at the start and end points were then applied to compute the total displacement vector $(\Delta\mathbf{R}_{\mathrm{GPS}})_{\mathrm{total}}$, which provides the reference relative position at the end of the trajectory. Difference between horizontal components of this reference position and a 2D laser/inertial relative position at the end of the trajectory ($(\Delta\mathbf{R}_{\mathrm{LS/INS}})_{\mathrm{total}}$) was applied to numerically characterize the positioning accuracy:

$$\delta R = \left\| \begin{bmatrix} (\Delta x_{GPS})_{total} \\ (\Delta y_{GPS})_{total} \end{bmatrix} \right\| - \left\| \begin{bmatrix} (\Delta x_{LS/INS})_{total} \\ (\Delta y_{LS/INS})_{total} \end{bmatrix} \right\| \qquad \text{Eq. 47}$$

where $\|.\|$ is the vector absolute value.

A value of δR can be considered as an upper error bound for the laser/INS integrated positioning. As mentioned previously, a position drift is created if new lines are added to a line list that is applied to compute the relative position. The integrated position solution thus drifts over distance as new lines are introduced into the line list. Maximum position error can be expected at the end of the trajectory. The difference between GPS and laser/inertial relative position at the end of the trajectory thus characterizes an upper error bound of the laser/INS integrated solution.

Similar to the indoor test case, laser scanner/inertial displacement residuals are applied to characterize the noise in the reconstructed trajectory.

Figure 18 illustrates a test trajectory that was implemented for the outdoor test scenario 1. It is important to note that outdoor scenarios normally impose significantly more challenges for the laser/inertial integrated navigation as compared to the indoor test case considered previously. Particularly, cases of poor line geometry can exist; e.g. for a case where a vehicle is driven between two parallel building walls, only parallel lines are extracted from scan images, which creates a singularity in the laser scanner-based position solution. Wall texture generally contributes significantly to line extraction errors. Finally, lines can remain in scan images for a limited duration only, especially for those cases where a vehicle is driven through a relatively open city street (i.e. a city street that has a limited number of buildings on it).

Trajectory reconstructed using the laser/inertial integrated position solution for the outdoor test scenario 1 is shown in Figure 19. The difference between the absolute value of the horizontal component of the kinematic GPS-derived total displacement vector and absolute value of the laser/inertial 2D displacement solution is calculated as follows:

$$\delta R = 198.38\ \text{m} - 199.95\ \text{m} = -1.57\ \text{m}$$

Errors in laser/inertial reconstructed trajectory are thus at the meter-level for the outdoor test scenario 1 (or 0.8% of the distance travelled).

Figure 20 shows laser inertial/displacement residuals.

Figure 18: Urban Outdoor Test Scenario 1

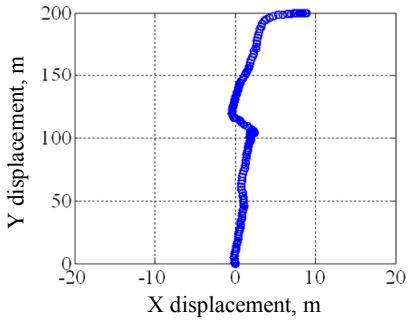

Figure 19: Outdoor Scenario 1: Integrated Laser Scanner/Inertial Reconstructed Trajectory

Residual standard deviations are evaluated as follows:

$$\left(\sigma_{\delta \mathbf{R}_{LS/INS}}\right)_x = 5.2\,\text{cm}$$
$$\left(\sigma_{\delta \mathbf{R}_{LS/INS}}\right)_y = 5.5\,\text{cm}$$

As it can be seen in Figure 20, there are regions for which residual values are not computed. These regions represent cases where lines extracted from scan images do not allow for a non-singular laser-based position solution.

Figure 21 shows the test trajectory for the urban outdoor test scenario 2. The laser/inertial reconstructed trajectory is represented in Figure 22. The difference between the absolute values of a 2D displacement vector at the trajectory completion computed from kinematic GPS data and laser/inertial data is computed as follows:

$$\delta R = 172.96\,\text{m} - 172.01\,\text{m} = 0.95\,\text{m}$$

Similar to the test scenario 1, relative position errors are found to be at the meter-level (or 0.6% of the distance travelled).

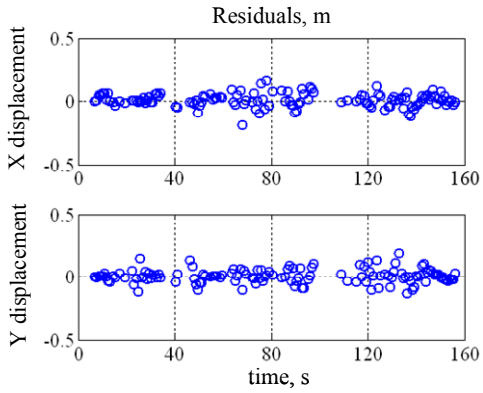

Figure 20: Outdoor Scenario 1: Laser Scanner/Inertial Displacement Residuals

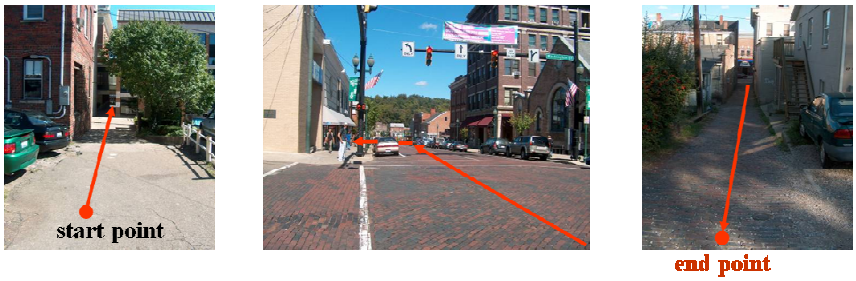

Figure 21: Urban Outdoor Test Scenario 2

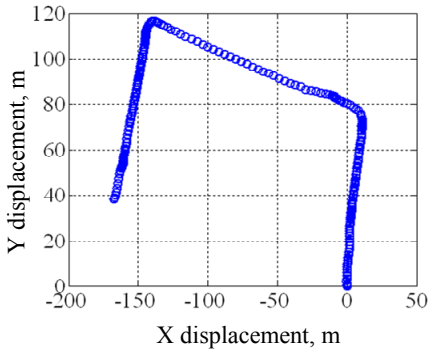

Figure 22: Outdoor Scenario 2: Integrated Laser Scanner/Inertial Reconstructed Trajectory

Laser/inertial residuals are shown in Figure 23.

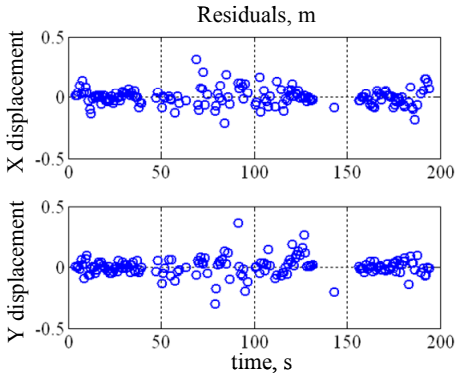

Figure 23: Outdoor Scenario 2: Laser Scanner/Inertial Displacement Residuals

Residual standard deviations are calculated as follows:

$$\left(\sigma_{\delta \mathbf{R}_{LS/INS}}\right)_x = 7.1\,\text{cm}$$
$$\left(\sigma_{\delta \mathbf{R}_{LS/INS}}\right)_y = 7.4\,\text{cm}$$

It is worth mentioning that both outdoor test scenarios implemented include portions with a relatively open sky (e.g. a portion of the trajectory shown in the upper photograph in Figure 21). It is thus expected that an augmentation of the laser/inertial integration with GNSS would improve the system performance. Such augmentation is thus recommended to be studied by future developments.

7.0 CONCLUSIONS

This paper develops a tightly coupled laser scanner/inertial navigation solution. The particular implementation case considered is a fully autonomous localization in a 2D relative coordinate frame that is defined by the laser scanner body frame at the initial scan. A tilt compensation algorithm introduced allows for an extension of a 2D case into a partial 3D case by removing constrains on the laser angular motion.

Estimating relative frame position and heading in one of commonly used navigation frames (e.g. East-North-Up and Earth-Centered-Earth-Fixed frames) allows for the transformation of the relative navigation solution developed herein into an absolute navigation solution. Particularly, GNSS measurements can be applied for relative/absolute navigation transformations if GNSS signals are available at the initial scan or one of the following scans.

SICK LMS-200 laser scanner data and Systron Donner DQI IMU data are used to demonstrate performance characteristics of the laser scanner/inertial integrated navigation for live data test cases. The particular test scenarios considered include indoor navigation through hallways of the Ohio University Stocker Engineering Center and outdoor navigation in urban alleys of Athens, Ohio. Cm-level position accuracy after 9 m of travel is demonstrated for indoor scenarios where well-defined features and good feature geometries are available. Test data from challenging urban environments show position errors at the meter-level after approx. 200 m of travel (between 0.6% and 0.8% of distance travelled).

8.0 ACKNOWLEDGEMENTS

This paper was previously presented at the Institute of Navigation's National Technical Meeting in San Diego, California in January 2007.

9.0 REFERENCES

[1] Altermatt M., Martinelli A., Tomatis N., Siegwart R., *SLAM with Corner Features Based on a Relative Map*. Proceedings of the International Conference on Intelligent Robots and Systems, Vol. 2, 2004.

[2] Borges G. A. and Aldon M.-J., *Line Extraction in 2D Range Images for Mobile Robotics*. Journal of Intelligent and Robotic Systems, Vol. 40, Issue 3, 2004.

[3] Pfister S., Roumeliotis S., Burdick J., *Weighted Line Fitting Algorithms for Mobile Robot Map Building and Efficient Data Representation*. Proceedings of the IEEE International Conference on Robotics and Automation, 2003.

[4] Pfister S., Kriechbaum K., Roumeliotis S., Burdick J., *Weighted Range Sensor Matching Algorithms for Mobile Robot Displacement Estimation*. Proceedings of the IEEE International Conference on Robotics and Automation (ICRA'02), 2002.

[5] Oskarsson M. and Astrom K., *Accurate and Automatic Surveying of Beacon Positions for a Laser Guided Vehicle*. Progress in Industrial Mathematics at ECMI 98, 1999.

[6] Bates D. P., *Navigation Using Optical Tracking of Objects at Unknown Locations*, Master's Thesis, Ohio University, March 2007.

[7] Diosi A. and Kleeman L., *Uncertainty of Line Segments Extracted from Static SICK PLS Laser Scans*. Proceedings of the Australian Conference on Robotics and Automation, 2003.

[8] Joerger M. and Pervan B., *Range-Domain Integration of GPS and Laser-scanner Measurements for Outdoor Navigation*. Proceedings of the ION GNSS, 2006.

[9] Nguyen V., Martinelli A., Tomatis N., Siegwar R., *A Comparison of Line Extraction Algorithms using 2D Laser Rangefinder for Indoor Mobile Robotics*. Proceedings of the IEEE Conference on Intelligent Robots and Systems, IROS, 2005.

[10] Titterton, D. H. and Weston J. L., *Strapdown Inertial Navigation Technology*, Second Edition, The American Institute of Aeronautics and Astronautics, Reston, Virginia, USA and The Institute of Electrical Engineers, Stevenage, UK, 2004.

[11] Brown, R. G. and Hwang, P. Y. C., Introduction to Random Signals and Applied Kalman Filtering, Third Edition, John Wiley & Sons, Inc., New York, 1997.

[12] Technical Description of the LMS 200, LMS 220, LMS 211, LMS 221, LMS 291 Laser Measurement Systems, Revised June 2003.
www.mysick.com/saqqara/pdf.aspx?id=im0012759

[13] Data sheet for DQI-digital quartz IMU.
www.systron.com/PDFS/datasheets/DQI.pdf

[14] OEM4 Family User Manual Volume 1: Installation and Operation. Revised December 22, 2005.
www.novatel.com/Documents/Manuals/om-20000046.pdf

[15] Spartan-3 Starter Kit Board User Guide.
www.xilinx.com/bvdocs/userguides/ug130.pdf

[16] Digilent PmodUSB2 Module Board Reference Manual.
www.digilentinc.com /Data/Products/USB2/ USB2_rm.pdf